Two-Dimensional Chromium Bismuthate: A Room-Temperature Ising Ferromagnet with Tunable Magneto-Optical Response

A. Mogulkoc,[1,*] M. Modarresi,[2] and A.N. Rudenko[3,4,†]

[1] *Department of Physics, Faculty of Sciences, Ankara University, Tandogan, Ankara 06100, Turkey*
[2] *Department of Physics, Ferdowsi University of Mashhad, Mashhad, Iran*
[3] *Radboud University, Institute for Molecules and Materials, Heyendaalseweg 135, Nijmegen 6525 AJ, Netherlands*
[4] *Department of Theoretical Physics and Applied Mathematics, Ural Federal University, Ekaterinburg 620002, Russia*

(Received 4 February 2021; revised 23 April 2021; accepted 1 June 2021; published 22 June 2021)

We present a density-functional-theory-based study of a two-dimensional phase of chromium bismuthate (CrBi), a previously unknown material with exceptional magnetic and magneto-optical characteristics. Monolayer CrBi is a ferromagnetic metal with strong spin-orbit coupling induced by the heavy bismuth atoms, resulting in a strongly anisotropic Ising-type magnetic ordering with the Curie temperature estimated to be higher than 300 K. The electronic structure of the system is topologically nontrivial, giving rise to a nonzero Berry curvature in the ground magnetic state, leading to the anomalous Hall effect with a conductivity plateau of about 1.5 e^2/h at the Fermi level. Remarkably, the Hall conductivity and the magneto-optical constant are found to be strongly dependent on the direction of magnetization. Besides, monolayer CrBi demonstrates the polar magneto-optical Kerr effect in the visible and near-ultraviolet spectral ranges with the maximum rotation angles of up to 10 mrad. Our findings suggest that monolayer CrBi is a promising system for practical applications in magneto-optical and spintronic devices.

DOI: 10.1103/PhysRevApplied.15.064053

I. INTRODUCTION

The discovery of graphene and its atom-thick analogues with unique electronic properties has attracted great interest in two-dimensional (2D) materials [1–4]. Recent experimental observation of magnetic order in 2D van der Waals crystals [5–11] was encouraging from both fundamental and practical points of view. In practice, 2D magnets offer exceptional tunability by means of applied voltage [12–15], mechanical strain [16–19], and stacking [5–7,20–22], and can be used as electrodes for prospective spintronic and magnetoresistance nanodevices [23–25]. The presence of magnetic order in two dimensions is a question of fundamental importance. Unlike three-dimensional magnets, long-range magnetic order in isotropic 2D magnets at finite temperatures is unstable with respect to thermal spin fluctuations [26,27]. The presence of an energy gap in the spectrum of spin-wave excitations is essential to stabilize the magnetic order in two dimensions, which is usually a direct consequence of magnetic anisotropy [28,29].

Experimental demonstration of 2D magnetism has triggered intensive theoretical research in this field. Theoretical studies are mainly focused on experimentally available materials, such as 2D chromium trihalides [15,22,30–36] and vanadium dichalcogenides [37–41]. On the other hand, quite a few 2D magnets have been predicted on the basis of first-principles calculations [42–53]. Among the large variety of 2D materials, one can distinguish materials with strong spin-orbit coupling (SOC), which is usually realized in heavy-element compounds. Apart from the fundamental interest, strong SOC provides additional control over materials' properties by means of electric [54,55] or magnetic fields [14], as well as playing a key role in the realization of topologically nontrivial phases [56]. In magnetic 2D materials, the effect of SOC is even more remarkable. First, it gives rise to magnetic anisotropy, which is responsible for the stabilization of long-range magnetic order in two dimensions [30]. Second, the breaking of time-reversal symmetry in combination with SOC affects the light-matter interaction, giving rise to anomalous transport properties [57,58] and to magneto-optical effects, such as the Faraday or Kerr rotation of the polarization angle [59–63]. Practically, the magneto-optical effect is a useful tool for the characterization of 2D magnetic materials. For example, magneto-optical measurements give insights into the variation of magnetic order from monolayer to multilayers [6]. On the other hand, magnetic materials with large Kerr or Faraday rotations are promising candidates

*mogulkoc@science.ankara.edu.tr
†a.rudenko@science.ru.nl

for potential magneto-optic devices such as controllable optical polarizers, modulators, switches, etc.

Recently, ferromagnetism has been predicted in 2D chromium pnictides [42,64,65]. This motivated us to consider another member of this family, namely, hexagonal monolayer CrBi. We show that the combination of strong SOC from the heavy bismuth atoms and the magnetic coupling between Cr atoms leads to exceptional properties of this material, such as room-temperature Ising-like ferromagnetism and tunable magneto-optical response. Specifically, we start from density functional theory (DFT) calculations, and investigate dynamical stability and electronic properties of monolayer CrBi. We then construct an effective anisotropic spin Hamiltonian and determine its parameters from first-principles calculations. We find that monolayer CrBi is a metallic ferromagnet with the easy axis normal to the 2D plane. Because of strong single-ion anisotropy, the system behaves like an Ising ferromagnet with a Curie temperature around 400 K. We also find that strong SOC gives rise to a nonzero Berry curvature, resulting in the anomalous Hall conductivity of about 1.5 e^2/h. Besides, our calculations show that monolayer CrBi demonstrates the magneto-optical Kerr effect in the visible spectral range with the rotation angles up to 10 mrad, which is strongly sensitive to the direction of magnetization.

The rest of the paper is organized as follows. In Sec. II, we briefly describe the theoretical model and computational details. In Sec. III A, we describe the atomic structure and assess the dynamical stability of monolayer CrBi. We then discuss the electronic structure (Sec. III B) and finite-temperature magnetism (Sec. III C). Section III D is devoted to the anomalous transport properties and their discussion. In Sec. III E, we analyze magneto-optical properties of monolayer CrBi. In the last section (Sec. IV), we briefly summarize our results.

II. METHOD AND COMPUTATIONAL DETAILS

A. First-principles calculations

The ground-state electronic structure calculations are performed within the *ab initio* methods based on DFT. We adopt the projected augmented wave (PAW) method [66,67] as implemented in the Vienna *ab initio* simulation package (VASP) [68,69]. The Brillouin zone (BZ) is sampled with a $(32 \times 32 \times 1)$ **k**-point mesh using the Monkhorst-Pack algorithm [70]. The kinetic energy cutoff for the plane-wave basis set is set to 800 eV. The exchange and correlation effects are described by using the generalized gradient approximation with the Perdew-Burke-Ernzerhof functional [71]. To capture the effects of strongly correlated electrons in atomic d orbitals, we use the DFT + U method [72,73], applying the effective on-site Coulomb repulsion to the d orbitals of Cr atoms. The value of the effective Hubbard-U parameter depends on the chemical structure and can be modulated by substrate dielectric screening and environment effects. Here we use $U = 3$ eV, which is a typical value for Cr-based compounds and consistent with previous DFT + U studies of Cr-based monolayer structures [30,64,74]. The lattice and atomic positions are optimized by using the conjugate gradient method to reach the ground-state energy configuration with a maximum 0.001 eV/Å force tolerance on each atom. The convergence criterion for the self-consistent solution of Kohn-Sham equations is set to 10^{-8} eV between two sequential steps. To avoid the interaction between periodic supercell images, we use a 30 Å vacuum distance along the nonperiodic z direction. The dynamical and thermal stability is examined by the calculation of phonon spectra and *ab initio* molecular dynamics (AIMD) simulations. The phonon spectra are obtained using the PHONOPY code [75] that is based on density functional perturbation theory, and using a $5 \times 5 \times 1$ supercell. The AIMD simulations are performed within the canonical ensemble (NVT) and Nosé-Hoover thermostat at $T =$ 300 K for a $4 \times 4 \times 1$ supercell with a time step of 2 fs. The charge distribution between Cr and Bi atoms is calculated using the Bader population analysis [76,77]. The side and top views of the CrBi hexagonal lattice (point group D_{3h}) are presented in Fig. 1(a).

The interband optical conductivity is calculated in the independent-particle approximation with the Kubo-Greenwood formula, which reads

$$\sigma_{\alpha\beta}^{\text{inter}}(\omega) = -\frac{ie^2\hbar}{N_k S}\sum_{\mathbf{k}}\sum_{n,m}\frac{f_{m\mathbf{k}} - f_{n\mathbf{k}}}{\varepsilon_{m\mathbf{k}} - \varepsilon_{n\mathbf{k}}} \times \frac{\langle\psi_{n\mathbf{k}}|v_\alpha|\psi_{m\mathbf{k}}\rangle\langle\psi_{m\mathbf{k}}|v_\beta|\psi_{n\mathbf{k}}\rangle}{\varepsilon_{m\mathbf{k}} - \varepsilon_{n\mathbf{k}} - (\hbar\omega - i\eta)}, \quad (1)$$

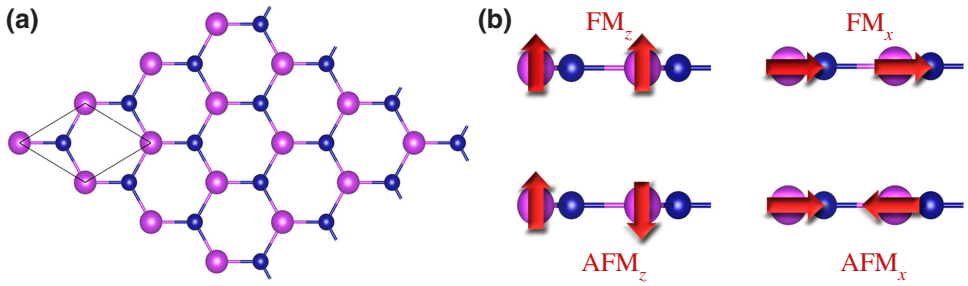

FIG. 1. The (a) top and (b) side views of relaxed monolayer CrBi together with the ferromagnetic (FM) and antiferromagnetic (AFM) configurations along the x and z directions. The purple and blue colors correspond to Cr and Bi atoms, respectively.

where α, β denote the Cartesian directions, S is the cell area, N_k is the number of $\mathbf{k}$ points used for BZ sampling, $f_{n\mathbf{k}} = f(\varepsilon_{n\mathbf{k}})$ is the Fermi-Dirac distribution function, and $v_{\alpha(\beta)}$ is the α (β) component of the group velocity operator defined in $\mathbf{k}$ space. Here ω is the optical frequency and $\eta = 0.01$ eV is an adjustable smearing parameter. The calculations are performed using the BERRY module [78,79] of the WANNIER90 package [80], which implements an efficient band interpolation technique by means of the maximally localized Wannier functions [81,82].

Taking into account the metallic character of CrBi, the intraband transitions should also be considered on top of the interband transition, which can be described by the conventional Drude term. The corresponding contribution to the diagonal components of the optical conductivity tensor is given by [83]

$$\sigma_{\alpha\alpha}^{\text{intra}}(\omega) = \varepsilon_0 \frac{h\omega_{\alpha,p}^2}{\gamma - i\omega}, \tag{2}$$

where γ is a damping term that is taken to be 0.01 eV, assuming the low scattering regime, and $\omega_{\alpha,p}$ is the α component of the effective plasma frequency,

$$\omega_{\alpha,p}^2 = -\frac{e^2}{Sh\varepsilon_0} \sum_{n,\mathbf{k}} \left(\frac{\partial f_{n\mathbf{k}}}{\partial \varepsilon_{n\mathbf{k}}} \right) |\langle \psi_{n\mathbf{k}} | v_\alpha | \psi_{n\mathbf{k}} \rangle|^2, \tag{3}$$

where we have introduced an effective layer thickness h. We assume that $h = 4.6$ Å for monolayer CrBi, considering the van der Waals radius of a Bi atom, which is 2.3 Å [84]. In what follows, the total optical conductivity is understood as the sum of the two terms, $\sigma_{\alpha\beta} = \sigma_{\alpha\beta}^{\text{intra}} + \sigma_{\alpha\beta}^{\text{inter}}$. The corresponding complex frequency-dependent dielectric function in the long-wavelength limit reads

$$\varepsilon_{\alpha\beta}(\omega) = \delta_{\alpha\beta} + \frac{i\sigma_{\alpha\beta}(\omega)}{h\omega\varepsilon_0}. \tag{4}$$

It is convenient to define the magneto-optical constant as

$$Q = \frac{i\varepsilon_{xy}^A}{\varepsilon_{xx}}, \tag{5}$$

where ε_{xy}^A is the asymmetric part of the off-diagonal component of the dielectric tensor.

In the limit of zero frequency $\omega \to 0$, the asymmetric off-diagonal component of the conductivity tensor corresponds to the anomalous Hall conductivity (AHC). It can be represented in terms of the z component of the Berry curvature $\Omega_{n,z}(\mathbf{k})$ as

$$\sigma_{xy}(0) = -\frac{e^2}{\hbar S} \sum_{n,\mathbf{k}} f_n(\mathbf{k}) \Omega_{n,z}(\mathbf{k}). \tag{6}$$

The Berry curvature is given by

$$\Omega_n(\mathbf{k}) = \nabla_{\mathbf{k}} \times \mathbf{A}_n(\mathbf{k}), \tag{7}$$

where $\mathbf{A}_n(\mathbf{k}) = \langle \psi_{n\mathbf{k}} | i\nabla_{\mathbf{k}} | \psi_{n\mathbf{k}} \rangle$ is the Berry connection defined in terms of cell-periodic Bloch states $|u_{n\mathbf{k}}\rangle = e^{i\mathbf{k}\cdot\mathbf{r}} |\psi_{n\mathbf{k}}\rangle$.

When polarized light is reflected from a ferromagnetic surface, its polarization state changes, which is the hallmark of the magneto-optical (polar) Kerr effect. The effect is characterized by the Kerr rotation (ϕ_K) and ellipticity (ψ_K) angles. In the limit $h \ll c\omega^{-1}$, i.e., when the material thickness is smaller compared to the photon wavelength, the following asymptotic expression is applicable for the case of normal incidence [85]:

$$\phi_K - i\psi_K = \frac{2nQ\omega h}{c(n^2 - 1)}. \tag{8}$$

Here $n = \sqrt{\varepsilon_s}$ is the refractive index of a substrate (SiO_2 $\varepsilon_s = 2.4$ [86]) and c is the speed of light.

B. Anisotropic spin model

The DFT results can be mapped onto the anisotropic classical spin model

$$H = -\sum_{i,j} J_{ij} \mathbf{S}_i \cdot \mathbf{S}_j - \sum_i D_i (\mathbf{S}_i \cdot \mathbf{z}_i)^2 - \sum_{i,j} \delta_{ij} S_i^z S_j^z, \tag{9}$$

where $J_{ij} \equiv J(\mathbf{R}_{ij})$ is the Heisenberg exchange interaction between spins $\mathbf{S}_i$ and $\mathbf{S}_j$, D_i is the single-ion magnetic anisotropy at spin $\mathbf{S}_i$, δ_{ij} is the anisotropic exchange interaction, and $\mathbf{z}_i$ is the unit vector pointing in the direction of the easy magnetization axis. Strictly speaking, Eq. (9) is justified for the atomic limit, i.e., when the Coulomb interaction between the Cr $3d$ electrons is larger compared to the $3d$ band width. We assume that this condition is fairly fulfilled in CrBi considering that the magnetization density is well localized on Cr atoms, leading to the integer magnetic moments. Nevertheless, we note that spin excitations resulting from Eq. (9) should be considered as approximate, which might lead, for instance, to overestimation of the critical temperatures.

For simplicity, we consider only nearest-neighbor exchange interactions in Eq. (9). The Mermin-Wagner-Hohenberg theorem states the absence of finite temperature phase transition for the isotropic Heisenberg Hamiltonian with short range interactions [26,27]. As a consequence, the anisotropy energy is crucially important for the stabilization of magnetic order in two dimensions [30,32,74].

In the hexagonal CrBi lattice each Cr atom has six nearest-neighbor Cr atoms. According to this model, the exchange coupling parameters can be expressed as [87]

$$J = (E_{\mathrm{AFM}_x} - E_{\mathrm{FM}_x})/16S^2, \tag{10a}$$

$$D = (E_{\mathrm{FM}_x} + 3E_{\mathrm{AFM}_x} - E_{\mathrm{FM}_z} - 3E_{\mathrm{AFM}_z})/4S^2, \tag{10b}$$

$$\delta = (E_{\mathrm{FM}_x} + E_{\mathrm{AFM}_z} - E_{\mathrm{FM}_z} - E_{\mathrm{AFM}_x})/16S^2, \tag{10c}$$

where E_{FM_x}, E_{FM_z}, E_{AFM_x}, and E_{AFM_z} are the total energies of FM_x, FM_z, AFM_x, and AFM_z configurations, respectively, shown in Fig. 1(b). The ground state of CrBi corresponds to a FM order with the magnetic moments $M = 3.0\mu_B$ localized on Cr atoms, which corresponds to $S = 3/2$. The spin operators in Hamiltonian (9) can be transformed into bosonic variables by means of linear spin-wave theory. The resulting spin-wave spectrum at zero temperature reads [88]

$$\omega(\mathbf{q}) = 2S[D + z\delta + J(0) - J(\mathbf{q})], \tag{11}$$

where $J(\mathbf{q})$ is the Fourier transform of $J(\mathbf{R}_{ij})$ and $z = 6$ is the number of nearest neighbors. The spin-wave spectrum has a gap $\Delta = 2S(D + z\delta)$, which stabilizes the 2D magnetic order. In the limit of a vanishing gap ($\Delta \to 0$), the long-range order at finite temperatures disappears, i.e., the ordering temperature $T_C \sim -1/\ln(\Delta) \to 0$ [74], in accordance with the Mermin-Wagner-Hohenberg theorem. In the presence of a dielectric substrate, the on-site Coulomb interaction on Cr atoms could be screened, leading to smaller U values. In order to understand the role of screening, J, δ, and D are calculated as a function of the Hubbard-U parameter and presented in Fig. S2 of the Supplemental Material [87]. It is known that next-nearest-neighbor exchange interactions can affect the Curie temperature in 2D magnets [89]. To check the effect of the second-nearest-neighbor exchange interaction in CrBi, we map the DFT results onto the Heisenberg Hamiltonian with J_1 and J_2 given in the Supplemental Material [87].

III. RESULTS AND DISCUSSION

A. Dynamical and thermal stability

We first examine the dynamical stability of the CrBi crystal structure by calculating the phonon spectrum presented in Fig. 2(a). There are three acoustic and three optical phonon branches. Around the Γ point the acoustic phonons are represented by two in-plane modes (LA and TA) with linear dispersion $\omega \sim |\mathbf{k}|$, and one flexural mode (ZA) with quadratic dispersion $\omega \sim \mathbf{k}^2$, which is typical of 2D materials [90]. The characteristic frequency of acoustic phonons, given by the frequencies at the edges of the BZ, appears at about 0.6 THz, and originates predominantly from the vibrations of Bi atoms [see the partial density of states in Fig. 2(a)]. In contrast, the optical phonons are characterized by essentially dispersionless modes mainly originating from Cr vibrations. There is one out-of-plane (ZO) and two in-plane (LO and TO) modes appearing around 1.5 and 5 THz, respectively. One can see the absence of imaginary modes in the entire BZ, which indicates stability of the crystal structure with respect to atomic vibrations. It is worth noting that the system may lose its stability in the presence of a highly dielectric environment (e.g., substrate), as demonstrated by our calculations performed without the Hubbard-U correction (not presented here).

We also analyze thermal stability of monolayer CrBi using the AIMD simulations carried out with the *NVT* ensemble at room temperature for a time period of 6 ps.

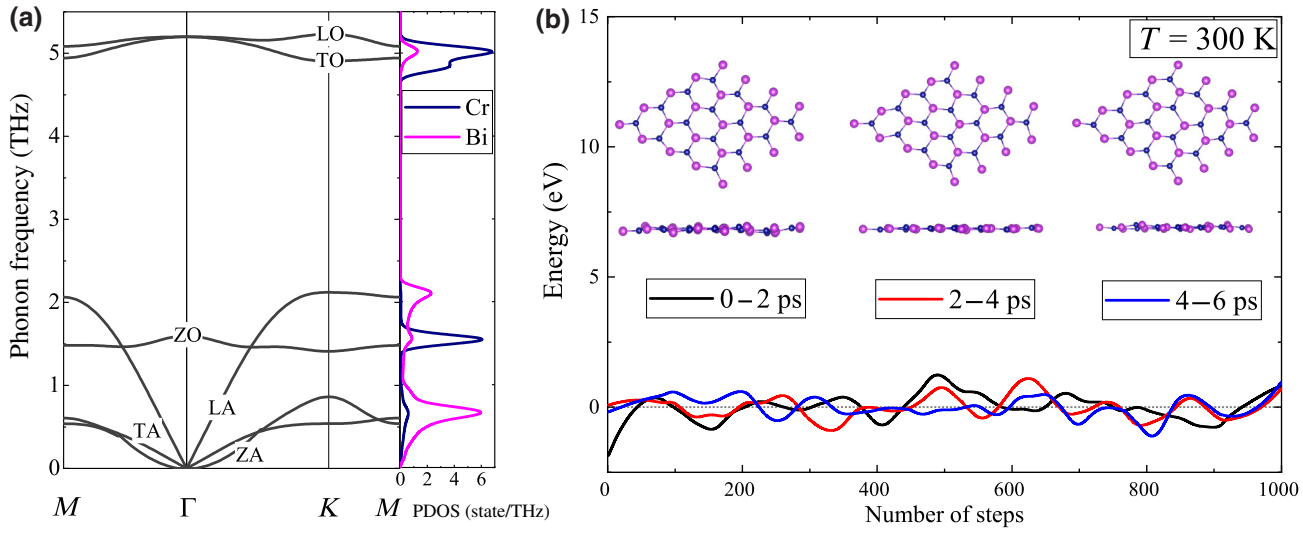

FIG. 2. (a) Phonon dispersion together with partial density of states (PDOS) calculated for monolayer CrBi with $U = 3$ eV. (b) Total energy obtained from the AIMD simulation performed over a period of 6 ps with *NVT* ensemble at $T = 300$ K.

The corresponding fluctuations of the total energy, as well as the structure snapshots taken every 2 ps, are presented in Fig. 2(b). One can see that the atomic structure remains stable and essentially flat at $T = 300$ K. Some distortions from the perfect hexagonal lattice are not large, and can be related to thermal fluctuations. The calculated root-mean-square displacement averaged over the last 1 ps results in $\sqrt{\langle|\mathbf{r}(t) - \mathbf{r}(0)|^2\rangle} \approx 0.21$ Å, whereas the averaged total energy fluctuation is around 30 meV/atom. This allows us to confirm thermal stability of monolayer CrBi at room temperature.

The structural parameters, cohesive energy, charge transfer, and work function of monolayer CrBi are summarized in Table I. The monolayer CrBi has no buckling with the lattice constant of 4.80 Å. The Bader population analysis [77] shows that there is a charge transfer from Cr to Bi around $0.6e$ that suggests a considerable ionic contribution to the bonding. The cohesive energy per unit cell of monolayer CrBi is around 3 eV, which is comparable with other monolayer chromium pnictides [42]. To characterize the photoelectric threshold, the work function is presented in Table I. The work function of CrBi is considerably smaller than in other 2D ferromagnets, such as chromium trihalides and vanadium dichalcogenides, where it is around 6 eV [91–93]. Thus, monolayer CrBi can be a good candidate for electrocatalysis applications, offering a low-energy barrier for the charge transfer. On the other hand, this may affect stability of the crystal structure in the presence of chemically reactive species.

TABLE I. The lattice constant (a), Cr—Bi bond length ($\ell_{Cr\text{—}Bi}$), charge transfer (ΔQ), cohesive energy (E_{coh}), and the work function (Φ_w). The calculations are performed with $U = 3$ eV. The work function is defined as $\Phi_w = E^{vac} - E_F$, where E^{vac} is the vacuum electrostatic potential, and E_F is the Fermi energy.

	a (Å)	$\ell_{Cr\text{—}Bi}$ (Å)	ΔQ ($\lvert e\rvert$)	E_{coh} (eV)	Φ_w (eV)
CrBi	4.80	2.77	0.57	3.11	3.13

B. Electronic structure

The electronic band structure of ferromagnetic monolayer CrBi calculated without and with SOC for the case when the magnetization is normal to the monolayer plane ($\mathbf{M} \parallel \mathbf{z}$) is presented in Figs. 3(a) and 3(b), respectively. In the absence of SOC, monolayer CrBi is a half-metal similar to other CrX (X = P, As, Sb) compounds [42]. The inclusion of SOC mixes spin-up and spin-down states, which is indicated by the color of the electronic bands in Fig. 3(b). Interestingly, the strongest effect of SOC is observed around the Fermi level, where one can see

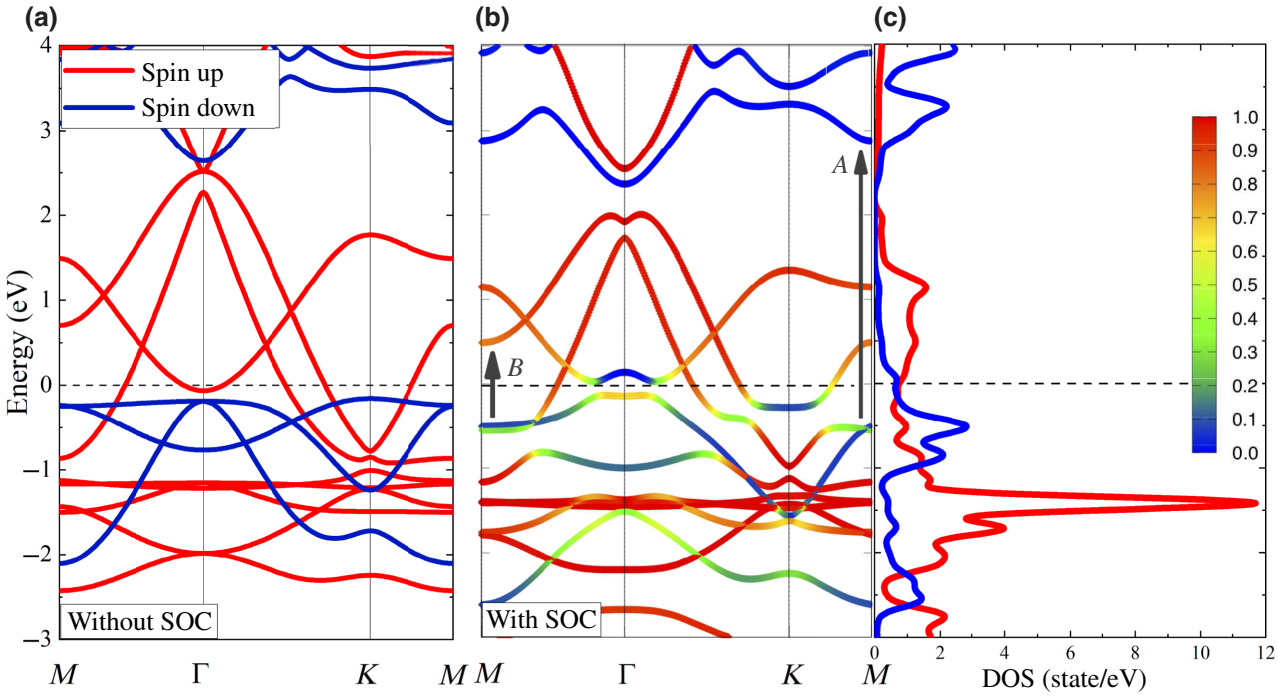

FIG. 3. Band structure of monolayer CrBi calculated (a) without and (b) with SOC. (c) The spin-projected DOS in the presence of SOC. The blue and red colors show the contributions of the spin-up and spin-down states. In both cases the direction of magnetization is normal to the monolayer plane ($\mathbf{M} \parallel \mathbf{z}$). The arrows indicate the most intensive optical transitions, giving rise to the two prominent absorption peaks shown in Fig. 4(c).

the largest mixing of spin-up and spin-down states. This results in a considerable modification of the electronic structure. In particular, from Fig. 3(b) one can see that the band inversion is taking place accompanied by the formation of a local SOC gap of 150 meV at avoided crossings. Remarkably, the Fermi energy lies within the gap, which suggests a topologically nontrivial character of the corresponding states. Although globally the system remains a trivial metal due to the presence of other bands crossing the Fermi energy, the SOC gap is expected to provide a considerable contribution to the anomalous transport properties. The spin decomposed density of electronic states for the SOC case is presented in Fig. 3(c). At the Fermi level, both spin-up and spin-down states contribute equally, which is in strong contrast with the half-metallic behavior observed without SOC. In other words, the half-metal to metal phase transition in monolayer CrBi is a manifestation of the strong SOC effect.

The situation when the magnetization is parallel to the monolayer plane ($\mathbf{M} \perp \mathbf{z}$) is different. Although the electronic bands are very similar for the z-axis magnetization [Fig. 3(b)] and x-axis magnetization (see the Supplemental Material [87]), there is an important difference at the Fermi level. Specifically, in the $\mathbf{M} \parallel \mathbf{z}$ case there is a SOC-induced local gap between the valence and conduction bands at the Γ point, while it is absent when $\mathbf{M} \perp \mathbf{z}$, and both bands are occupied. As we discuss below in Sec. III D, the presence of the corresponding gap produces a net Berry curvature around the Γ point.

C. Finite-temperature magnetism

As a next step, we examine the magnetic properties of monolayer CrBi at the level of the anisotropic spin Hamiltonian given by Eq. (9). In order to determine the model parameters, we estimate the total energies of different magnetic configurations shown in Fig. 1(b), using noncollinear DFT + U + SOC calculations. The CrBi monolayer is found to have a FM ground state with the easy axis normal to the plane. The magnetic moment is well localized on Cr atoms, and has the value of $3.0\mu_B$ per cell, which corresponds to the spin $S = 3/2$. The parameters J, D, and δ are determined via Eqs. (10), where we restricted ourselves to the nearest-neighbor exchange interactions. Despite the metallic character of CrBi, the next-nearest-neighbor interactions are smaller [87], not affecting the results presented below. The resulting calculated parameters are $J = 1.59$ meV, $D = 8.51$ meV, and $\delta = 0.63$ meV, summarized in Table II. In contrast to the isostructural compounds CrX (X = P, As, Sb) [42], the isotropic exchange interaction J in CrBi is considerably smaller. This can be attributed to a larger lattice constant, which suppresses the FM contribution to the exchange interaction, according to the model proposed in Ref. [33]. On the other hand, the single-ion anisotropy D is significantly larger, which is due to the strong SOC of bismuth. One can see that $D \gg \delta$, i.e., the magnetic anisotropy mainly arises from the single-ion term. Although both parameters are related to SOC, they have distinct physical origins. While the anisotropic exchange δ is of kinetic origin [94], single-ion anisotropy D can be attributed to the formation of local orbital moments [95]. Furthermore, one can see that $J \ll D$, which suggests that monolayer CrBi is an Ising-type ferromagnet. Indeed, in this regime spin fluctuations with nonzero S_x and S_y projections are highly unfavorable. Therefore, we can recast the spin Hamiltonian as $H \approx -\sum_{\langle ij \rangle} J_{ij}^{\text{eff}} S_i^z S_j^z$, which is the Ising Hamiltonian with nearest-neighbor interactions $J_{ij}^{\text{eff}} = 2(J_{ij} + \delta_{ij})$. We note that the variation of the parameters with the Hubbard U does not change the Ising-type behavior of monolayer CrBi [87].

TABLE II. The isotropic exchange interaction between nearest-neighbor spins (J), single-ion anisotropy energy (D), intersite anisotropy parameter (δ), net magnetization per Cr atom (M), and the Curie temperature (T_C). The calculations are performed with $U = 3$ eV.

	J (meV)	D (meV)	δ (meV)	M (μ_B)	T_C (K)
CrBi	1.59	8.51	0.63	3.0	420[a] (600[b])

[a]Ising model.
[b]RPA scheme.

The critical temperature of the 2D Ising model on a triangular lattice is known exactly, which is $k_B T_C = 4J^{\text{eff}} S^2/\ln 3$ [96]. It is worth noting that the Ising model is intrinsically anisotropic, and thus compatible with the Mermin-Wagner-Hohenberg theorem. In our case the Ising model yields $T_C \simeq 420$ K. This value is expected to be somewhat overestimated because of finite D, and because of the ignored next-nearest-neighbor interactions, which are small but tend to destabilize the FM ordering [42]. Nevertheless, we expect T_C to be of the order of room temperature, which is larger than for recently proposed 2D Ising ferromagnet VI_3 [97] with $T_C \sim 100$ K. The high T_C in CrBi is not only related to a strong exchange coupling between Cr spins, but can be also attributed to the relatively large spin $S = 3/2$ and to a larger coordination number ($z = 6$) compared to materials with the honeycomb lattice. It is interesting to note that a T_C estimation within the RPA approach [42,98] based on Tyablikov's decoupling approximation yields even larger $T_C \simeq 600$ K (see the Supplemental Material [87] for details). However, this scheme is apparently inapplicable in the regime $D \gg J$, as demonstrated in Ref. [96]. The inclusion of the second-nearest-neighbor exchange interaction in the spin model does not lead to any significant changes of the Curie temperature, as we show in the Supplemental Material [87].

D. Anomalous Hall conductivity

For a crystal with inversion symmetry, the Berry curvature obeys $\Omega_n(\mathbf{k}) = \Omega_n(-\mathbf{k})$, while time-reversal symmetry implies that $\Omega_n(\mathbf{k}) = -\Omega_n(-\mathbf{k})$, which means that $\Omega_n(\mathbf{k}) = 0$ for a crystal with both inversion and time-reversal symmetries. In the case of a magnetic monolayer, the Berry curvature may be nonzero, which is related to spontaneously broken time-reversal symmetry. Additionally, spin mixing is required to ensure a nonzero Berry curvature, which is induced by SOC. All these conditions are fulfilled in monolayer CrBi.

Figure 4(a) shows the low-energy electronic bands in monolayer CrBi. Around the Γ point the bands are inverted with a local SOC gap. At the points, where the band crossing is avoided, one can see the emergence of two strong peaks of the same sign in the Berry curvature [lower panel in Fig. 4(a)]. Interestingly, if CrBi is magnetized along the in-plane (x) direction, the band topology around the Fermi energy changes such that the contribution to the Berry curvature around Γ vanishes [87]. In Fig. 4(b), we show the anomalous Hall conductivity, which exhibits a plateau equal to about 1.5 e^2/h at the Fermi level. The width of the plateau is about 0.2 eV, which makes it robust against perturbations, such as structural and charge disorder, and allows for experimental detection. The AHC plateau at the Fermi level is equivalent to about 200 S/cm, which is comparable to experimental measurements for Heusler alloys [99] and layered iron-doped TaS_2 [100], but almost an order of magnitude smaller than in pure Fe, Ni, Co, and Gd films [101]. It should be emphasized that in our case AHC is not quantized because the system remains a trivial metal even in the presence of SOC. The integer (quantum) AHC was theoretically reported in CrI_3 [102], iron trihalides [32], and $CoBr_2$ [103] monolayers.

In Fig. 4(b), one can see another AHC plateau of around $-0.5\ e^2/h$ at about 0.3 eV below the Fermi energy. Interestingly, AHC switches its sign for the chemical potentials around −0.2 and 0.1 eV. In practice, the variation of the chemical potential can be achieved by the electron or hole doping. Strong sensitivity of AHC to moderate

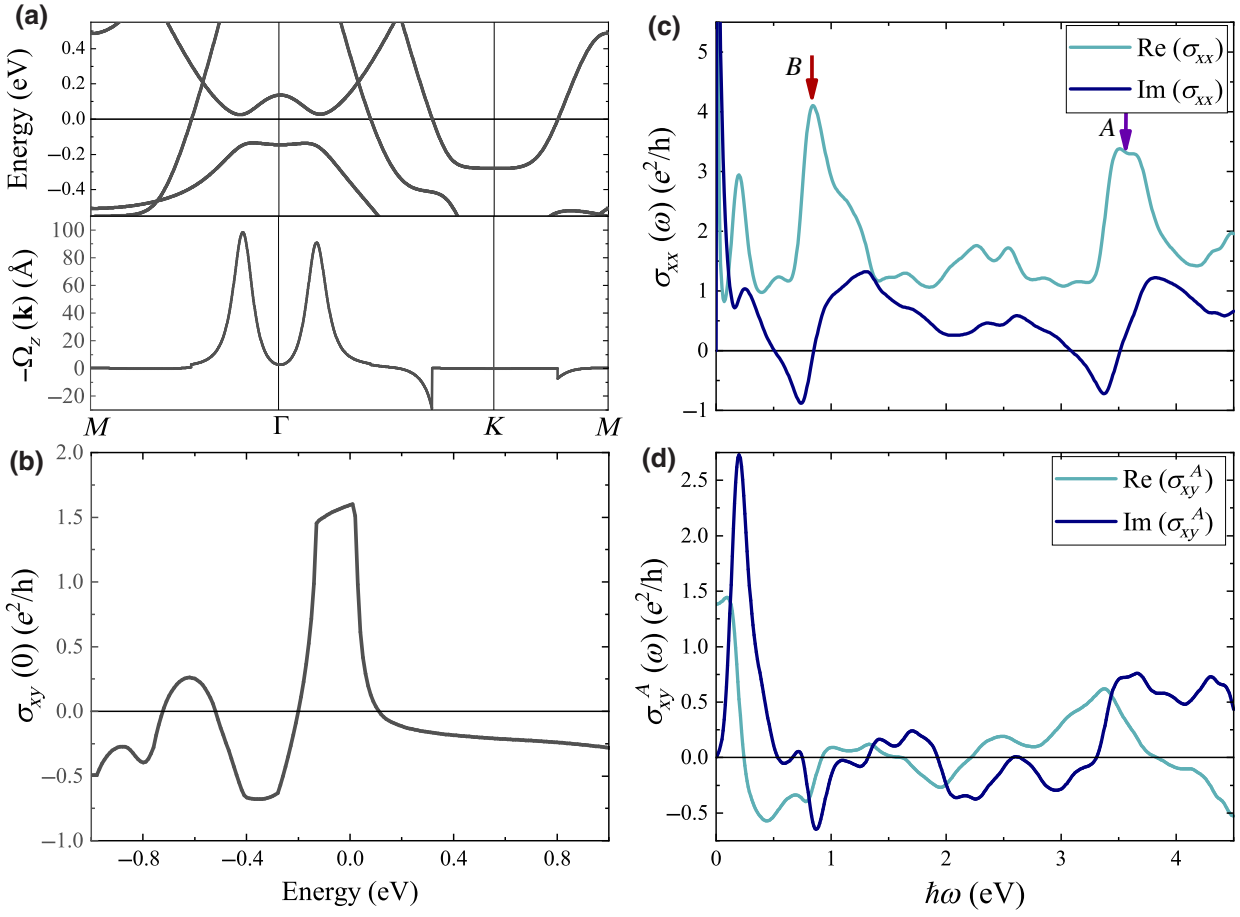

FIG. 4. (a) The electronic bands around the Fermi level and the Berry curvature along the high-symmetry points in the BZ. (b) The anomalous Hall conductivity of monolayer CrBi calculated as a function of the energy (chemical potential). (c) Diagonal and (d) asymmetric off-diagonal components of the frequency-dependent optical conductivity. In all cases the out-of-plane magnetization (**M** ∥ **z**) of monolayer CrBi is assumed.

charge doping can be regarded as a peculiarity of monolayer CrBi, and can be utilized to verify our findings experimentally. Another prominent characteristic of AHC in monolayer CrBi is its dependence on the magnetization direction. Although the z direction of magnetization is the ground state of the monolayer CrBi direction, the magnetic moments can be aligned in plane upon application of an external magnetic field. In this situation, AHC is almost zero for all practically relevant chemical potentials [87]. These results are promising for the realization of the *tunable* anomalous Hall effect by means of an external magnetic field.

E. Magneto-optical response

The real and imaginary parts of the diagonal component of the optical conductivity $\sigma_{xx}(\omega)$ are shown in Fig. 4 (c) as a function of the photon energy. Because of the metallic character of CrBi, one can see a Drude peak appearing in the low-frequency range, originating from the intraband transitions included in the form of Eq. (2). The optical spectrum exhibits two prominent absorption peaks around about 0.8 and 3.5 eV placed at mid-infrared (mid-IR) and near-ultraviolet (near-UV) regions, which can be directly related to the interband transitions. The corresponding transitions are shown in Fig. 3(b), denoted by the letters A and B. Figure 4(d) shows the frequency dependence of the asymmetric off-diagonal component of the conductivity, $\sigma^{A}_{xy}(\omega)$. A nonzero σ^{A}_{xy} is conditioned by the absence of time-reversal symmetry and the presence of SOC. At about 0.25 eV the real part has a strong peak, which can be associated with the SOC-induced gap in the band structure [Fig. 3(b)], and with the spin mixture of the corresponding bands at the Fermi energy. Importantly, this peak is absent in the case of in-plane magnetization ($\mathbf{M} \perp \mathbf{z}$) because the corresponding spin-mixed states are fully occupied (see the Supplemental Material [87]).

The magneto-optical (Voigt) constant $Q(\omega)$ arising from the off-diagonal terms of the dielectric tensor [see Eq. (5)] gives information about the magneto-optical activity. In Fig. 5(a), we present $Q(\omega)$ calculated for two directions of magnetization in monolayer CrBi. For the out-of-plane ($\mathbf{M} \parallel \mathbf{z}$) magnetization, $Q(\omega)$ exhibits a strong peak around the IR region, similar to that observed in Fig. 4(d). On the other hand, for the in-plane ($\mathbf{M} \perp \mathbf{z}$) magnetization, $Q(\omega)$ is almost 10^3 times smaller. A similar trend is observed in the visible part of the spectrum. Therefore, the magneto-optical activity of monolayer CrBi

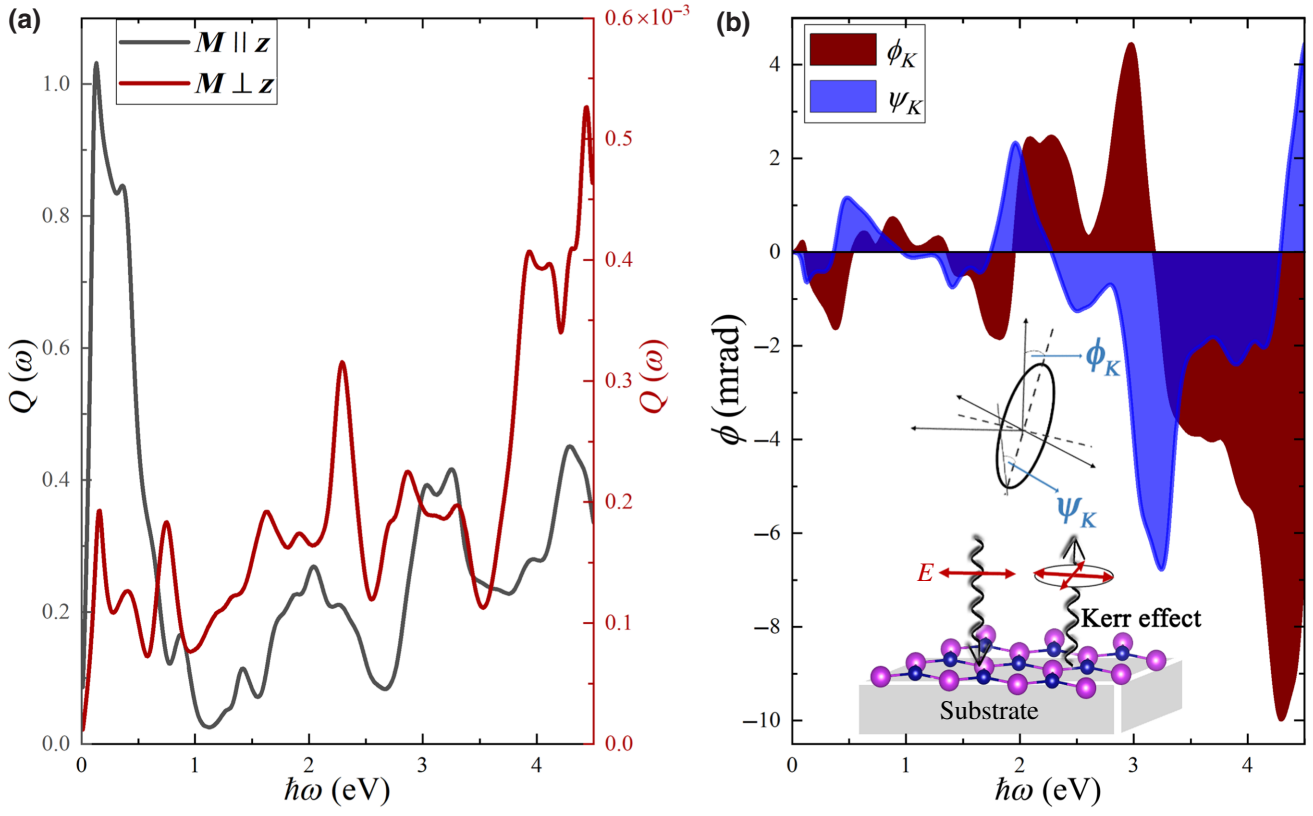

FIG. 5. (a) The magneto-optical constant as a function of the photon energy for the out-of-plane ($\mathbf{M} \parallel \mathbf{z}$) magnetization and in-plane ($\mathbf{M} \perp \mathbf{z}$) magnetization (note the different scales). (b) The Kerr rotation (ϕ_K) (red) and the Kerr ellipticity (ψ_K) (blue) angles calculated as a function of the photon energy for the out-of-plane ($\mathbf{M} \parallel \mathbf{z}$) magnetization. In the calculations, we assume a SiO_2 substrate with the dielectric constant $\varepsilon_s = 2.4$. Inset: schematic illustration of the polar magneto-optical Kerr effect at normal incidence.

is strongly dependent on the direction of magnetization, and almost negligible in the case of in-plane magnetization. We note that this is a direct consequence of the magnetization-dependent electronic structure modification, and not related to the angle of incidence.

The Kerr rotation angles are calculated using Eq. (8) and presented as a function of the photon energy in Fig. 5(b) for the out-of-plane magnetization ($\mathbf{M} \parallel \mathbf{z}$) and normal incidence. In our calculations we assume the presence of a SiO_2 substrate with the dielectric constant $\varepsilon_s = 2.4$. As one can see from Fig. 5(b), for the out-of-plane magnetization (red shaded curve), the Kerr rotation spectrum (ϕ_K) exhibits a few peaks in the visible part of the electromagnetic spectrum with the magnitude up to 4.4 mrad (0.25°). The same order of rotation angles can be seen in the Kerr ellipticity spectrum (ψ_K). The Kerr rotation and ellipticity spectra both have a prominent peak in the near-UV region with magnitudes of -10 mrad ($-0.57°$) and -6.8 mrad ($-0.38°$), respectively. The calculated rotation angles are smaller, but comparable with those in ferromagnetic monolayer CrI_3 [59–61], where the magneto-optical Kerr effect is pronounced. We note that the magnitudes of ϕ_K and ψ_K could be increased by a factor $\varepsilon_s - 1$ in the free-standing monolayer.

It should be noted that in our calculations we ignore nonlocal correlation effects, responsible for the formation of bound electron-hole states. These effects are important for insulators and semiconductors because they determine the optical gap. Furthermore, reduced dielectric screening of 2D materials usually enhances the binding energies of excitons. However, in our case we deal with a metallic system, implying that the screening effects are large. In this situation, we do not expect that many-body perturbative corrections (e.g., at the *GW* level) would significantly modify our results. Nevertheless, we admit that a more sophisticated many-body treatment of electronic correlations would be desirable to support our findings. This problem is left for future research.

IV. CONCLUSION

In summary, we have systematically studied the electronic, magnetic, and magneto-optical properties of hexagonal monolayer CrBi using first-principles calculations. As a first step, we demonstrate that the crystal structure of monolayer CrBi is dynamically stable at room temperature. We then show that, due to the heavy bismuth atoms, the system exhibits strong SOC, giving rise to a strong single-ion anisotropy. This allows us to consider monolayer CrBi as a 2D Ising ferromagnet, whose Curie temperature is estimated to be above 300 K. From the electronic structure point of view, monolayer CrBi is a metal. Strong SOC affects topology of the electronic bands, leading to a nonzero Berry curvature. This results in the anomalous Hall effect with AHC of about 1.5 e^2/h at the Fermi energy. Finally, we consider the magneto-optical response of monolayer CrBi and find considerable Kerr rotation angles of up to 10 mrad in the visible and near-UV spectral ranges. The magneto-optical response as well as AHC can be effectively tuned by changing the magnetization direction and, therefore, make monolayer CrBi a promising candidate for practical applications. We believe that our findings could be verified experimentally, and will be useful for future theoretical and experimental studies of 2D magnetic materials.

ACKNOWLEDGMENTS

The authors acknowledge the Ankara University for high performance computing facility through the AYP under Grant No. 17A0443001. This work is supported by the Scientific and Technological Research Council of Turkey (TUBITAK) under Project No. 119F361. The numerical calculations reported in this paper were partially performed at TUBITAK ULAKBIM, High Performance and Grid Computing Center (TRUBA resources).

[1] T. Wang, M. Park, Q. Yu, J. Zhang, and Y. Yang, Stability and synthesis of 2D metals and alloys: A review, Mater. Today Adv. **8**, 100092 (2020).

[2] A. Zavabeti, A. Jannat, L. Zhong, A. A. Haidry, Z. Yao, and J. Z. Ou, Two-dimensional materials in large-areas: Synthesis, properties and applications, Nano-Micro Lett. **12**, 66 (2020).

[3] K. Khan, A. K. Tareen, M. Aslam, R. Wang, Y. Zhang, A. Mahmood, Z. Ouyang, H. Zhang, and Z. Guo, Recent developments in emerging two-dimensional materials and their applications, J. Mater. Chem. C **8**, 387 (2020).

[4] M. Bernardi, C. Ataca, M. Palummo, and J. C. Grossman, Optical and electronic properties of two-dimensional layered materials, Nanophotonics **6**, 479 (2017).

[5] C. Gong, L. Li, Z. Li, H. Ji, A. Stern, Y. Xia, T. Cao, W. Bao, C. Wang, Y. Wang, *et al.*, Discovery of intrinsic ferromagnetism in two-dimensional van der Waals crystals, Nature **546**, 265 (2017).

[6] B. Huang, G. Clark, E. Navarro-Moratalla, D. R. Klein, R. Cheng, K. L. Seyler, D. Zhong, E. Schmidgall, M. A. McGuire, D. H. Cobden, *et al.*, Layer-dependent ferromagnetism in a van der Waals crystal down to the monolayer limit, Nature **546**, 270 (2017).

[7] W. Chen, Z. Sun, Z. Wang, L. Gu, X. Xu, S. Wu, and C. Gao, Direct observation of van der Waals stacking–dependent interlayer magnetism, Science **366**, 983 (2019).

[8] M. Bonilla, S. Kolekar, Y. Ma, H. C. Diaz, V. Kalappattil, R. Das, T. Eggers, H. R. Gutierrez, M.-H. Phan, and M. Batzill, Strong room-temperature ferromagnetism in VSe_2 monolayers on van der Waals substrates, Nat. Nanotechnol. **13**, 289 (2018).

[9] D. J. O'Hara, T. Zhu, A. H. Trout, A. S. Ahmed, Y. K. Luo, C. H. Lee, M. R. Brenner, S. Rajan, J. A. Gupta,

D. W. McComb, *et al.*, Room temperature intrinsic ferromagnetism in epitaxial manganese selenide films in the monolayer limit, Nano Lett. **18**, 3125 (2018).

[10] T. Hattori, T. Miyamachi, T. Yokoyama, and F. Komori, Electronic and magnetic properties of the Fe_2N monolayer film tuned by substrate symmetry, J. Phys. Condens. Matter **31**, 255001 (2019).

[11] Y. Deng, Y. Yu, Y. Song, J. Zhang, N. Z. Wang, Z. Sun, Y. Yi, Y. Z. Wu, S. Wu, J. Zhu, *et al.*, Gate-tunable room-temperature ferromagnetism in two-dimensional Fe_3GeTe_2, Nature **563**, 94 (2018).

[12] B. Huang, G. Clark, D. R. Klein, D. MacNeill, E. Navarro-Moratalla, K. L. Seyler, N. Wilson, M. A. McGuire, D. H. Cobden, D. Xiao, *et al.*, Electrical control of 2D magnetism in bilayer CrI_3, Nat. Nanotechnol. **13**, 544 (2018).

[13] Z. Wang, T. Zhang, M. Ding, B. Dong, Y. Li, M. Chen, X. Li, J. Huang, H. Wang, X. Zhao, *et al.*, Electric-field control of magnetism in a few-layered van der Waals ferromagnetic semiconductor, Nat. Nanotechnol. **13**, 554 (2018).

[14] S. Jiang, L. Li, Z. Wang, K. F. Mak, and J. Shan, Controlling magnetism in 2D CrI_3 by electrostatic doping, Nat. Nanotechnol. **13**, 549 (2018).

[15] E. Suárez Morell, A. León, R. H. Miwa, and P. Vargas, Control of magnetism in bilayer CrI_3 by an external electric field, 2D Mater. **6**, 025020 (2019).

[16] Z. Wu, J. Yu, and S. Yuan, Strain-tunable magnetic and electronic properties of monolayer CrI_3, Phys. Chem. Chem. Phys. **21**, 7750 (2019).

[17] Z. Guan, N. Luo, S. Ni, and S. Hu, Tunable electronic and magnetic properties of monolayer and bilayer Janus $Cr_2Cl_3I_3$: A first-principles study, Mater. Adv. **1**, 244 (2020).

[18] H. Y. Lv, W. J. Lu, X. Luo, X. B. Zhu, and Y. P. Sun, Strain- and carrier-tunable magnetic properties of a two-dimensional intrinsically ferromagnetic semiconductor: $CoBr_2$ monolayer, Phys. Rev. B **99**, 134416 (2019).

[19] R. Albaridy, A. Manchon, and U. Schwingenschlögl, Tunable magnetic anisotropy in Cr–trihalide Janus monolayers, J. Phys. Condens. Matter **32**, 355702 (2020).

[20] P. Jiang, L. Li, Z. Liao, Y. X. Zhao, and Z. Zhong, Spin direction-controlled electronic band structure in two-dimensional ferromagnetic CrI_3, Nano Lett. **18**, 3844 (2018).

[21] N. Sivadas, S. Okamoto, X. Xu, C. J. Fennie, and D. Xiao, Stacking-dependent magnetism in bilayer CrI_3, Nano Lett. **18**, 7658 (2018).

[22] D. Soriano, C. Cardoso, and J. Fernández-Rossier, Interplay between interlayer exchange and stacking in CrI_3 bilayers, Solid State Commun. **299**, 113662 (2019).

[23] D. R. Klein, D. MacNeill, J. L. Lado, D. Soriano, E. Navarro-Moratalla, K. Watanabe, T. Taniguchi, S. Manni, P. Canfield, J. Fernández-Rossier, *et al.*, Probing magnetism in 2D van der Waals crystalline insulators via electron tunneling, Science **360**, 1218 (2018).

[24] T. Song, X. Cai, M. W.-Y. Tu, X. Zhang, B. Huang, N. P. Wilson, K. L. Seyler, L. Zhu, T. Taniguchi, K. Watanabe, *et al.*, Giant tunneling magnetoresistance in spin-filter van der Waals heterostructures, Science **360**, 1214 (2018).

[25] Z. Wang, I. Gutiérrez-Lezama, N. Ubrig, M. Kroner, M. Gibertini, T. Taniguchi, K. Watanabe, A. Imamoglu, E. Giannini, and A. F. Morpurgo, Very large tunneling magnetoresistance in layered magnetic semiconductor CrI_3, Nat. Commun. **9**, 2516 (2018).

[26] N. D. Mermin and H. Wagner, Absence of Ferromagnetism or Antiferromagnetism in One- or Two-Dimensional Isotropic Heisenberg Models, Phys. Rev. Lett. **17**, 1133 (1966).

[27] P. C. Hohenberg, Existence of long-range order in one and two dimensions, Phys. Rev. **158**, 383 (1967).

[28] P. Bruno, Spin-wave theory of two-dimensional ferromagnets in the presence of dipolar interactions and magnetocrystalline anisotropy, Phys. Rev. B **43**, 6015 (1991).

[29] V. Y. Irkhin, A. A. Katanin, and M. I. Katsnelson, Self-consistent spin-wave theory of layered Heisenberg magnets, Phys. Rev. B **60**, 1082 (1999).

[30] J. L. Lado and J. Fernández-Rossier, On the origin of magnetic anisotropy in two dimensional CrI_3, 2D Mater. **4**, 035002 (2017).

[31] L. Webster and J.-A. Yan, Strain-tunable magnetic anisotropy in monolayer $CrCl_3$, $CrBr_3$, and CrI_3, Phys. Rev. B **98**, 144411 (2018).

[32] P. Li, Prediction of intrinsic two dimensional ferromagnetism realized quantum anomalous Hall effect, Phys. Chem. Chem. Phys. **21**, 6712 (2019).

[33] I. V. Kashin, V. V. Mazurenko, M. I. Katsnelson, and A. N. Rudenko, Orbitally-resolved ferromagnetism of monolayer CrI_3, 2D Mater. **7**, 025036 (2020).

[34] Y. O. Kvashnin, A. Bergman, A. I. Lichtenstein, and M. I. Katsnelson, Relativistic exchange interactions in CrX_3 ($X = \mathrm{Cl}, \mathrm{Br}, \mathrm{I}$) monolayers, Phys. Rev. B **102**, 115162 (2020).

[35] A. K. Behera, S. Chowdhury, and S. R. Das, Magnetic skyrmions in atomic thin CrI_3 monolayer, Appl. Phys. Lett. **114**, 232402 (2019).

[36] S. Tiwari, M. L. Van de Put, B. Sorée, and W. G. Vandenberghe, Critical behavior of the ferromagnets CrI_3, $CrBr_3$ and $CrGeTe_3$ and the antiferromagnet $FeCl_2$: A detailed first-principles study, Phys. Rev. B **103**, 014432 (2021).

[37] M. Esters, R. G. Hennig, and D. C. Johnson, Dynamic instabilities in strongly correlated VSe_2 monolayers and bilayers, Phys. Rev. B **96**, 235147 (2017).

[38] G. V. Pushkarev, V. G. Mazurenko, V. V. Mazurenko, and D. W. Boukhvalov, Structural phase transitions in VSe_2: Energetics, electronic structure and magnetism, Phys. Chem. Chem. Phys. **21**, 22647 (2019).

[39] N. Luo, C. Si, and W. Duan, Structural and electronic phase transitions in ferromagnetic monolayer VS_2 induced by charge doping, Phys. Rev. B **95**, 205432 (2017).

[40] J. Zhou, J. Qiao, C.-G. Duan, A. Bournel, K. L. Wang, and W. Zhao, Large tunneling magnetoresistance in VSe_2/MoS_2 magnetic tunnel junction, ACS Appl. Mater. Interfaces **11**, 17647 (2019).

[41] E. B. Isaacs and C. A. Marianetti, Electronic correlations in monolayer VS_2, Phys. Rev. B **94**, 035120 (2016).

[42] A. Mogulkoc, M. Modarresi, and A. N. Rudenko, Two-dimensional chromium pnictides CrX ($X = \mathrm{P}, \mathrm{As}, \mathrm{Sb}$): Half-metallic ferromagnets with high Curie temperature, Phys. Rev. B **102**, 024441 (2020).

[43] R. Han, Z. Jiang, and Y. Yan, Prediction of novel 2D intrinsic ferromagnetic materials with high curie temperature and large perpendicular magnetic anisotropy, J. Phys. Chem. C **124**, 7956 (2020).

[44] Z. Chen, X. Fan, Z. Shen, Z. Luo, D. Yang, and S. Ma, Two-dimensional intrinsic ferromagnetic half-metals: Monolayers Mn_3X_4 ($X = \mathrm{Te}, \mathrm{Se}, \mathrm{S}$), J. Mater. Sci. **55**, 7680 (2020).

[45] J. Liu, Z. Liu, T. Song, and X. Cui, Computational search for two-dimensional intrinsic half-metals in transition-metal dinitrides, J. Mater. Chem. C **5**, 727 (2017).

[46] B. G. Li, Y. F. Zheng, H. Cui, P. Wang, T. W. Zhou, D. D. Wang, H. Chen, and H. K. Yuan, First-principles investigation of a new 2D magnetic crystal: Ferromagnetic ordering and intrinsic half-metallicity, J. Chem. Phys. **152**, 244704 (2020).

[47] Q. Chen, Q. Ding, Y. Wang, Y. Xu, and J. Wang, Electronic and magnetic properties of a two-dimensional transition metal phosphorous chalcogenide $TMPS_4$, J. Phys. Chem. C **124**, 12075 (2020).

[48] S. Chen, F. Wu, Q. Li, H. Sun, J. Ding, C. Huang, and E. Kan, Prediction of room-temperature ferromagnetism in a two-dimensional direct band gap semiconductor, Nanoscale **12**, 15670 (2020).

[49] K. Choudhary, K. F. Garrity, J. Jiang, R. Pachter, and F. Tavazza, Computational search for magnetic and non-magnetic 2D topological materials using unified spin–orbit spillage screening, npj Comput. Mater. **6**, 1 (2020).

[50] S. Haastrup, M. Strange, M. Pandey, T. Deilmann, P. S. Schmidt, N. F. Hinsche, M. N. Gjerding, D. Torelli, P. M. Larsen, A. C. Riis-Jensen, *et al.*, The computational 2D materials database: High-throughput modeling and discovery of atomically thin crystals, 2D Mater. **5**, 042002 (2018).

[51] T. D. Rhone, W. Chen, S. Desai, S. B. Torrisi, D. T. Larson, A. Yacoby, and E. Kaxiras, Data-driven studies of magnetic two-dimensional materials, Sci. Rep. **10**, 1 (2020).

[52] I. Miyazato, Y. Tanaka, and K. Takahashi, Accelerating the discovery of hidden two-dimensional magnets using machine learning and first principle calculations, J. Phys. Condens. Matter **30**, 06LT01 (2018).

[53] P. D. Reyntjens, S. Tiwari, M. L. Van de Put, B. Sorée, and W. G. Vandenberghe, Magnetic properties and critical behavior of magnetically intercalated WSe_2: A theoretical study, 2D Mater. **8**, 025009 (2020).

[54] D. A. Prishchenko, V. G. Mazurenko, M. I. Katsnelson, and A. N. Rudenko, Gate-tunable infrared plasmons in electron-doped single-layer antimony, Phys. Rev. B **98**, 201401(R) (2018).

[55] A. V. Lugovskoi, M. I. Katsnelson, and A. N. Rudenko, Electron-phonon properties, structural stability, and superconductivity of doped antimonene, Phys. Rev. B **99**, 064513 (2019).

[56] M. Z. Hasan and C. L. Kane, Colloquium: Topological insulators, Rev. Mod. Phys. **82**, 3045 (2010).

[57] N. Nagaosa, J. Sinova, S. Onoda, A. H. MacDonald, and N. P. Ong, Anomalous Hall effect, Rev. Mod. Phys. **82**, 1539 (2010).

[58] C.-X. Liu, S.-C. Zhang, and X.-L. Qi, The quantum anomalous Hall effect: Theory and experiment, Annu. Rev. Condens. Matter Phys. **7**, 301 (2016).

[59] M. Wu, Z. Li, T. Cao, and S. G. Louie, Physical origin of giant excitonic and magneto-optical responses in two-dimensional ferromagnetic insulators, Nat. Commun. **10**, 2371 (2019).

[60] V. K. Gudelli and G.-Y. Guo, Magnetism and magneto-optical effects in bulk and few-layer CrI_3: A theoretical GGA + U study, New J. Phys. **21**, 053012 (2019).

[61] A. Molina-Sánchez, G. Catarina, D. Sangalli, and J. Fernández-Rossier, Magneto-optical response of chromium trihalide monolayers: Chemical trends, J. Mater. Chem. C **8**, 8856 (2020).

[62] G. Catarina, N. M. R. Peres, and J. Fernández-Rossier, Magneto-optical kerr effect in spin split two-dimensional massive dirac materials, 2D Mater. **7**, 025011 (2020).

[63] K. Yang, W. Hu, H. Wu, M.-H. Whangbo, P. G. Radaelli, and A. Stroppa, Magneto-optical kerr switching properties of $(CrI_3)_2$ and $(CrBr_3/CrI_3)$ bilayers, ACS Appl. Electron. Mater. **2**, 1373 (2020).

[64] A. V. Kuklin, A. A. Kuzubov, E. A. Kovaleva, N. S. Mikhaleva, F. N. Tomilin, H. Lee, and P. V. Avramov, Two-dimensional hexagonal CrN with promising magnetic and optical properties: A theoretical prediction, Nanoscale **9**, 621 (2017).

[65] G. Rahman and Z. Jahangirli, Cras monolayer: Low buckled 2D half-metal ferromagnet, Phys. Status Solidi RRL **14**, 1900509 (2019).

[66] P. E. Blöchl, Projector augmented-wave method, Phys. Rev. B **50**, 17953 (1994).

[67] G. Kresse and D. Joubert, From ultrasoft pseudopotentials to the projector augmented-wave method, Phys. Rev. B **59**, 1758 (1999).

[68] G. Kresse and J. Furthmüller, Efficiency of ab-initio total energy calculations for metals and semiconductors using a plane-wave basis set, Comput. Mater. Sci. **6**, 15 (1996).

[69] G. Kresse and J. Furthmüller, Efficient iterative schemes for *ab initio* total-energy calculations using a plane-wave basis set, Phys. Rev. B **54**, 11169 (1996).

[70] H. J. Monkhorst and J. D. Pack, Special points for Brillouin-zone integrations, Phys. Rev. B **13**, 5188 (1976).

[71] J. P. Perdew, K. Burke, and M. Ernzerhof, Generalized Gradient Approximation Made Simple, Phys. Rev. Lett. **77**, 3865 (1996).

[72] V. I. Anisimov, F. Aryasetiawan, and A. I. Lichtenstein, First-principles calculations of the electronic structure and spectra of strongly correlated systems: The LDA + U method, J. Phys.: Condens. Matter **9**, 767 (1997).

[73] S. L. Dudarev, G. A. Botton, S. Y. Savrasov, C. J. Humphreys, and A. P. Sutton, Electron-energy-loss spectra and the structural stability of nickel oxide: An LSDA + U study, Phys. Rev. B **57**, 1505 (1998).

[74] M. Modarresi, A. Mogulkoc, Y. Mogulkoc, and A. Rudenko, Lateral Spin Valve Based on the Two-Dimensional CrN/P/CrN Heterostructure, Phys. Rev. Appl. **11**, 064015 (2019).

[75] A. Togo, L. Chaput, and I. Tanaka, Distributions of phonon lifetimes in Brillouin zones, Phys. Rev. B **91**, 094306 (2015).

[76] W. Tang, E. Sanville, and G. Henkelman, A grid-based Bader analysis algorithm without lattice bias, J. Phys.: Condens. Matter **21**, 084204 (2009).

[77] G. Henkelman, A. Arnaldsson, and H. Jónsson, A fast and robust algorithm for Bader decomposition of charge density, Comput. Mater. Sci. **36**, 354 (2006).

[78] X. Wang, J. R. Yates, I. Souza, and D. Vanderbilt, Ab initio calculation of the anomalous Hall conductivity by Wannier interpolation, Phys. Rev. B **74**, 195118 (2006).

[79] Y. Yao, L. Kleinman, A. H. MacDonald, J. Sinova, T. Jungwirth, D.-s. Wang, E. Wang, and Q. Niu, First Principles Calculation of Anomalous Hall Conductivity in Ferromagnetic bcc Fe, Phys. Rev. Lett. **92**, 037204 (2004).

[80] A. A. Mostofi, J. R. Yates, Y.-S. Lee, I. Souza, D. Vanderbilt, and N. Marzari, wannier90: A tool for obtaining maximally-localised Wannier functions, Comput. Phys. Commun. **178**, 685 (2008).

[81] N. Marzari and D. Vanderbilt, Maximally localized generalized Wannier functions for composite energy bands, Phys. Rev. B **56**, 12847 (1997).

[82] N. Marzari, A. A. Mostofi, J. R. Yates, I. Souza, and D. Vanderbilt, Maximally localized Wannier functions: Theory and applications, Rev. Mod. Phys. **84**, 1419 (2012).

[83] A. Fox and D. Fox, *Optical Properties of Solids*, Oxford Master Series in Condensed Matter Physics (Oxford University Press, New York, 2001).

[84] M. Mantina, A. C. Chamberlin, R. Valero, C. J. Cramer, and D. G. Truhlar, Consistent van der Waals radii for the whole main group, J. Phys. Chem. A **113**, 5806 (2009).

[85] A. K. Zvezdin and V. A. Kotov, *Modern Magnetooptics and Magnetooptical Materials* (CRC Press, Bristol, 1997).

[86] W. Wolf, S. Stanley, and K. McCarty, *American Institute Handbook of Physics* (McGraw-Hill, New York, 1963).

[87] See Supplemental Material at http://link.aps.org/supplemental/10.1103/PhysRevApplied.15.064053 for (i) parameters of the anisotropic spin model, (ii) the Curie temperature in the random phase approximation, and (iii) the anomalous Hall conductivity and magneto-optical response for the case of in-plane magnetization.

[88] S. Memarzadeh, M. Rezaei Roknabadi, M. Modarresi, A. Mogulkoc, and A. N. Rudenko, Role of charge doping and strain in the stabilization of in-plane ferromagnetism in monolayer VSe_2 at room temperature, 2D Mater. **8**, 035022 (2021).

[89] J. Vanherck, C. Bacaksiz, B. Sorée, M. V. Miloševic, and W. Magnus, 2D ferromagnetism at finite temperatures under quantum scrutiny, Appl. Phys. Lett. **117**, 052401 (2020).

[90] A. N. Rudenko, A. V. Lugovskoi, A. Mauri, G. Yu, S. Yuan, and M. I. Katsnelson, Interplay between in-plane and flexural phonons in electronic transport of two-dimensional semiconductors, Phys. Rev. B **100**, 075417 (2019).

[91] J. Du, C. Xia, W. Xiong, T. Wang, Y. Jia, and J. Li, Two-dimensional transition-metal dichalcogenides-based ferromagnetic van der Waals heterostructures, Nanoscale **9**, 17585 (2017).

[92] Z.-L. Liu, X. Wu, Y. Shao, J. Qi, Y. Cao, L. Huang, C. Liu, J.-O. Wang, Q. Zheng, Z.-L. Zhu, K. Ibrahim, Y.-L. Wang, and H.-J. Gao, Epitaxially grown monolayer VSe_2: An air-stable magnetic two-dimensional material with low work function at edges, Sci. Bull. **63**, 419 (2018).

[93] H. Li, Y.-K. Xu, K. Lai, and W.-B. Zhang, The enhanced ferromagnetism of single-layer CrX_3 (X = Br and I) via van der Waals engineering, Phys. Chem. Chem. Phys. **21**, 11949 (2019).

[94] T. Yildirim, A. B. Harris, A. Aharony, and O. Entin-Wohlman, Anisotropic spin Hamiltonians due to spin-orbit and coulomb exchange interactions, Phys. Rev. B **52**, 10239 (1995).

[95] P. Bruno, Tight-binding approach to the orbital magnetic moment and magnetocrystalline anisotropy of transition-metal monolayers, Phys. Rev. B **39**, 865 (1989).

[96] D. Torelli and T. Olsen, Calculating critical temperatures for ferromagnetic order in two-dimensional materials, 2D Mater. **6**, 015028 (2018).

[97] K. Yang, F. Fan, H. Wang, D. I. Khomskii, and H. Wu, VI3: A two-dimensional Ising ferromagnet, Phys. Rev. B **101**, 100402(R) (2020).

[98] J. Rusz, I. Turek, and M. Diviš, Random-phase approximation for critical temperatures of collinear magnets with multiple sublattices: GdX compounds (X = Mg, Rh, Ni, Pd), Phys. Rev. B **71**, 174408 (2005).

[99] A. Husmann and L. J. Singh, Temperature dependence of the anomalous Hall conductivity in the Heusler alloy Co_2CrAl, Phys. Rev. B **73**, 172417 (2006).

[100] J. G. Checkelsky, M. Lee, E. Morosan, R. J. Cava, and N. P. Ong, Anomalous Hall effect and magnetoresistance in the layered ferromagnet $Fe_1/4TaS_2$: The inelastic regime, Phys. Rev. B **77**, 014433 (2008).

[101] T. Miyasato, N. Abe, T. Fujii, A. Asamitsu, S. Onoda, Y. Onose, N. Nagaosa, and Y. Tokura, Crossover Behavior of the Anomalous Hall Effect and Anomalous Nernst Effect in Itinerant Ferromagnets, Phys. Rev. Lett. **99**, 086602 (2007).

[102] M. Zhu, H. Yao, L. Jiang, and Y. Zheng, Theoretical model of spintronic device based on tunable anomalous Hall conductivity of monolayer CrI_3, Appl. Phys. Lett. **116**, 022404 (2020).

[103] P. Chen, J.-Y. Zou, and B.-G. Liu, Intrinsic ferromagnetism and quantum anomalous Hall effect in a $CoBr_2$ monolayer, Phys. Chem. Chem. Phys. **19**, 13432 (2017).